Available online at www.sciencedirect.com
ScienceDirect
Journal of the European Ceramic Society 27 (2007) 2153–2161
www.elsevier.com/locate/jeurceramsoc

The effect of different sintering additives on the electrical and oxidation properties of Si_3N_4–$MoSi_2$ composites

Zhiquan Guo [a], Gurdial Blugan [a], Thomas Graule [a], Mike Reece [b], Jakob Kuebler [a,*]

[a] *Empa, Material Science and Technology, Laboratory for High Performance Ceramics, Ueberlandstrasse 129, Duebendorf CH-8600, Switzerland*
[b] *Queen Mary, University of London, Mile End Road, London E2 4NS, UK*

Received 22 April 2006; received in revised form 28 June 2006; accepted 7 July 2006
Available online 11 September 2006

Abstract

The fabrication and properties of electrically conductive Si_3N_4–$MoSi_2$ composites using two different sintering additive systems were investigated (i) Y_2O_3–Al_2O_3 and (ii) Lu_2O_3. It was found that the sintering atmosphere used (N_2 or Ar) had a critical influence on the final phase composition because $MoSi_2$ reacted with N_2 atmosphere during sintering resulting in the formation of Mo_5Si_3. The electrical conductivity of the composites exhibited typical percolation type behaviour and the percolation concentrations depended on the type of sintering additive and atmosphere used. Metallic-like conduction was the dominant conduction mechanism in the composites with $MoSi_2$ content over the percolation concentrations due to the formation of a three-dimensional percolation network of the conductive $MoSi_2$ phase. The effect of the sintering additives on the electrical and oxidation properties of the composites at elevated temperatures was investigated. Parabolic oxidation kinetics was observed in the composites with both types of additives. However, the Lu_2O_3-doped composites had superior oxidation resistance compared to the composites containing Y_2O_3–Al_2O_3. It is attributed to the higher eutectic temperature and crystallisation of the grain boundary phase and the oxidation layer in the Lu_2O_3-doped composites.

Keywords: Hot pressing; Composites; Electrical conductivity; Si_3N_4; Sintering additives

1. Introduction

Silicon nitride (Si_3N_4) is an important high-temperature structural ceramic due to its combination of excellent oxidation resistance and high strength at elevated temperatures. However, the widespread application of Si_3N_4 materials is limited by their relatively low fracture toughness when compared to metals. Another major barrier is the cost of manufacture. Since Si_3N_4-based materials possess high hardness,[1] hence expensive diamond machining is normally required to produce Si_3N_4-based components. The addition of particulate reinforcements to Si_3N_4 can increase the toughness of the materials by mechanisms including residual stresses generated by the mismatch of coefficients of thermal expansion (CTE), crack bridging and crack deflection.[2,3]

The inclusion of a certain amount of electroconductive particles into the insulating Si_3N_4 matrix can lead to electrically conductive composites, this can facilitate machining of these composites into complex shapes by the more economical electrical discharge machining (EDM).[4] Various Si_3N_4 composites with addition of an electroconductive secondary phase, such as TiN,[3] TiB_2,[5] TaN,[6,7] TiC[8] and $MoSi_2$,[9,10] have been studied. Among them, Si_3N_4–$MoSi_2$ composites are of special interest. $MoSi_2$ is a high-melting-point (2030 °C) intermetallic material with high electrical conductivity ($\sim 2 \times 10^5\ \Omega^{-1}\ cm^{-1}$ at room temperature). $MoSi_2$ has superior high-temperature oxidation resistance compared with the other aforementioned reinforcement phases. It has been reported that the presence of $MoSi_2$ phase in a Si_3N_4 matrix leads to a better oxidation resistance compared with monolithic Si_3N_4.[11] According to a study of Klemm et al.,[12] the formation of a Si_2N_2O layer underneath the surface as an oxidation product is responsible for the improvement of oxidation resistance. Si_3N_4–$MoSi_2$ composites have great potential for high-temperature electrical applications. For instance, it has been used as heating elements of ceramic glow plugs for diesel engines.[13] However, only limited data on the electrical conductivity of Si_3N_4–$MoSi_2$ composites is available in the literature.[13,14]

* Corresponding author. Tel.: +41 44 8234223; fax: +41 44 8234150.
E-mail address: jakob.kuebler@empa.ch (J. Kuebler).

0955-2219/$ – see front matter © 2006 Elsevier Ltd. All rights reserved.
doi:10.1016/j.jeurceramsoc.2006.07.009

Si_3N_4 is a highly covalent material and has low self-diffusivity. Full densification of Si_3N_4 ceramics cannot be achieved by conventional solid state sintering. Usually rare-earth (RE) oxides, e.g. Y_2O_3,[15] Yb_2O_3,[16] Sm_2O_3[16] and Gd_2O_3,[16] or oxide mixtures, e.g. Y_2O_3–Al_2O_3[17] and Y_2O_3–SiO_2,[18] are used as sintering aids to promote the densification by liquid phase sintering. This can lead to amorphous grain boundary phases being formed from the remaining liquid phase upon cooling. The nature of the grain boundary phase effectively controls their mechanical properties and oxidation resistance at elevated temperatures.[17,19,20] It was reported recently that Si_3N_4 doped with Lu_2O_3 as the sintering additive shows the best oxidation resistance[21] and the highest strength at 1500 °C[22] ever reported for Si_3N_4 materials. This is closely associated with the crystallisation of the grain boundary phase.[23] It can be expected that the use of Lu_2O_3 as the sintering additive for Si_3N_4–$MoSi_2$ composites can also improve the oxidation resistance and high-temperature properties.

In this work, we report the fabrication of two different Si_3N_4–$MoSi_2$ composites, using (i) Y_2O_3–Al_2O_3 (YAG) and (ii) Lu_2O_3 as sintering additives. Their electrical conductivity at temperatures up to 1250 °C and the oxidation behaviour at 1500 °C were studied.

2. Experimental procedure

Si_3N_4–$MoSi_2$ composites with up to 60 vol.% $MoSi_2$ were synthesized using commercial Si_3N_4 (grade M11, H.C. Starck, Germany) and $MoSi_2$ (grade C, H.C. Starck, Germany) powders. Two types of composites with different sintering additives were prepared: Si_3N_4–$MoSi_2$–$Y_2O_3 + Al_2O_3$, designated as SMY, and Si_3N_4–$MoSi_2$–Lu_2O_3, designated as SML. For the SMY composites, 1.5 vol.% Al_2O_3 (CT3000 SG, Bassermann Minerals, Germany) and 3.5 vol.% Y_2O_3 (grade C, H.C. Starck, Germany) were used as the sintering additives. For the SML composites, 5 vol.% Lu_2O_3 (99.9% pure, Metall Rare Earth Ltd., China) was added to the starting powders as the sintering aid. The starting powders were mixed in isopropanol by a planetary mill (PM400, Retsch) for 4 h. Additionally 1 wt.% polyvinyl butyral (PVB) (Mowital B 20H, Clariant GmbH, Germany) as binder was added to the dispersion after the milling process. The wet powder mixture was then dried in a rotary evaporator and passed through a 200 μm sieve. This precursor powder was compacted by uniaxial pressing to produce disc-shaped green bodies with a diameter of 20 mm. The powder compacts were sintered in BN-coated graphite dies by hot pressing (Model 383-40, Thermal Technology Inc.) under a mechanical pressure of 30 MPa in 1 atm N_2 or Ar atmosphere. Due to the different eutectic temperatures of Y_2O_3–Al_2O_3–SiO_2 and Lu_2O_3–SiO_2, different sintering temperatures were used in the SMY and SML composites. The sintering temperatures were 1700 °C for the SMY composites and 1800 °C for the SML composites.

The densities of the sintered composites were measured by Archimedes method. It was found that all the produced materials were >98% of their theoretical density. Specimens were polished and plasma etched for the microstructural analysis using a scanning electron microscopy (SEM) (VEGA TS 5136 Tescan, CZ). The grain diameter was measured using the linear intercept method as described in EN 623-3 standard.[24] The room-temperature electrical conductivity of the composites was determined by the van der Pauw method.[25] The high-temperature dc electrical conductivity of Si_3N_4–$MoSi_2$ composites was measured using a four-probe method in accordance with ASTM standard F43-93.[26] Disc-shaped specimens with 18 mm in diameter and 2 mm in thickness were used for the oxidation tests. The oxidation experiments were carried out at 1500 °C in air with a heating/cooling rate of 5 °C/min in an electrical resistance furnace (FHT 1750, Ceram-Aix, Germany). The specimens were removed from the furnace at intervals of 1, 1, 2, 4, 8, 16, 32 and 64 h for weighing on an analytical balance with an accuracy of ±0.001 mg (MX/UMX, Mettler Toledo, Switzerland). X-ray diffraction (XRD) (PANalytical PW 3040/60 X'Pert PRO) was used to determine the crystalline phases of both as-sintered and oxidized specimens.

3. Results and discussion

3.1. Phase compositions and microstructure

The Si_3N_4–$MoSi_2$ composites containing YAG or Lu_2O_3 as sintering additives were consolidated by hot-pressing in Ar or N_2 atmospheres. The phase compositions of the resultant composites are shown in Fig. 1. The XRD spectra indicate that the selection of the sintering atmospheres (Ar or N_2) has a critical influence on the final phase compositions. The SMY composites consolidated in Ar atmosphere contained β-Si_3N_4 and $MoSi_2$ phases. No crystallised grain boundary phase was observed. However, when N_2 was used as the sintering atmosphere, Mo_5Si_3 phase, instead of $MoSi_2$ phase, was identified. These results indicate that $MoSi_2$ reacted with N_2 atmosphere to form Mo_5Si_3 during the sintering process. The possible reaction is proposed by the following equation:

$$15MoSi_2(s) + 14N_2(g) \rightarrow 3Mo_5Si_3(s) + 7Si_3N_4(s) \quad (1)$$

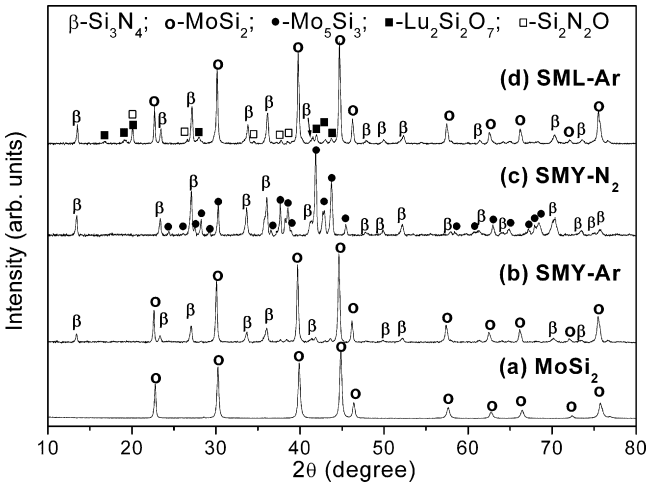

Fig. 1. X-ray diffraction patterns of (a) $MoSi_2$ powder, the Si_3N_4–$MoSi_2$ composites with $Y_2O_3 + Al_2O_3$ additives (SMY) sintered in (b) Ar or (c) N_2; (d) the Si_3N_4–$MoSi_2$–Lu_2O_3 composite (SML) sintered in Ar.

In the literature, Si_3N_4–$MoSi_2$ composites are normally consolidated by hot-pressing at temperatures from 1650 to 1840 °C in Ar,[10] N_2[27] or vacuum.[14] It was reported in all of these studies that Si_3N_4 and $MoSi_2$ are thermodynamically stable. Our findings contradict the results found by Kao,[27] who did not notice any reaction or decomposition of the compacts of Si_3N_4 and $MoSi_2$ powders during hot-pressing at 1650 °C in 1 atm N_2. To understand our results, the thermodynamics of the reaction needs to be considered. Using the thermodynamic data given by Barin and Platzki,[28] the Gibbs free energy changes ΔG_1° (kJ mol^{-1}) of Eq. (1) can be obtained as a function of temperature (°C) using the following equation:

$$\Delta G_1^\circ = -4276.8 + 2.1555T \quad (2)$$

This calculation indicates that in 1 atm N_2 atmosphere, the Gibbs free energy change ΔG_1° is negative at temperatures lower than 1711.13 °C, and hence the reaction (Eq. (1)) should proceed towards the right-side and form Mo_5Si_3 and Si_3N_4 phases. Therefore, our results are supported by the prediction of this thermodynamic calculation. According to the study of the Mo–Si_3N_4 system by Heikinheimo et al.[29], $MoSi_2$ phase is in equilibrium with Si_3N_4 at low N_2 partial pressure ($\sim 10^{-4}$ bar) at 1300 °C. However, the formation of Mo_5Si_3 is thermodynamically favourable at N_2 partial pressure between 0.03 and 7 bar. This may explain why the reaction did not occur during the sintering of Si_3N_4–$MoSi_2$ composites in an Ar atmosphere.

The XRD pattern of the Lu_2O_3-doped Si_3N_4–$MoSi_2$ composites, which was sintered in Ar, is also shown in Fig. 1. The four crystalline phases identified from the XRD pattern were β-Si_3N_4, $MoSi_2$, $Lu_2Si_2O_7$ and Si_2N_2O. $Lu_2Si_2O_7$ and Si_2N_2O were crystallised as secondary phases. They were formed from the reaction of Lu_2O_3, Si_3N_4 and SiO_2, the latter is always present on the surface of the Si_3N_4 and $MoSi_2$ powders. The possible reaction is given in the following equation:

$$Lu_2O_3 + Si_3N_4 + 3SiO_2 \rightarrow Lu_2Si_2O_7 + 2Si_2N_2O \quad (3)$$

It has been reported that Si_3N_4 doped with lanthanide rare-earth oxides (RE_2O_3, RE = Sm, Gd, Dy, Er and Yb) also contains $RE_2Si_2O_7$ and Si_2N_2O as the grain boundary phases.[16] Since the electronic configuration in all lanthanide ions (RE^{3+}), including Lu^{3+}, is very similar, the chemistry within these group is very similar as well.[16] Therefore, the reaction as described by Eq. (3) is expected. Compared to Y_2O_3–Al_2O_3 (YAG) sintering additives, which resulted in amorphous boundary phase, Lu_2O_3 produced grain boundary phase with extensive crystallization,[23] which improves the material properties including high-temperature strength and oxidation resistance.[21,22]

The microstructures of the composites with 40 vol.% $MoSi_2$ are shown in Fig. 2. The brighter grains were $MoSi_2$ (or Mo_5Si_3) particles and the darker grains were the Si_3N_4 matrix. Fig. 2(a) and (b) were obtained from the composites produced using the same starting powder (Si_3N_4–40 vol.% $MoSi_2$–YAG), but sintered in different atmospheres: N_2 for Fig. 2(a) and Ar for Fig. 2(b). It was found that the resultant volume fraction of the Mo_5Si_3 phase in the composite sintered in N_2 was significantly smaller than that of the $MoSi_2$ phase in the composite sintered in Ar. The volume fraction of the remaining Mo_5Si_3 phase in the composites sintered in N_2 was roughly 20 vol.%, i.e. only half of the $MoSi_2$ volume fraction in the starting powder. This can be explained by the reaction (Eq. (1)) of $MoSi_2$ and N_2 during the sintering process, resulting in formation of additional Si_3N_4 in the composite. The Mo_5Si_3 is also an electrical conductor ($\sim 10^{-5}$ Ω cm), however the resulting volume fraction of the Mo_5Si_3 conductive phase in the composite sintered in N_2 was below the percolation concentration, which is approximately 30 vol.% for Si_3N_4–$MoSi_2$ composites.[14] This leads to a very high resistivity (>10^{10} Ω cm) of the composite sintered in N_2, while the composite sintered in Ar was a good conductor ($\sim 10^{-3}$ Ω cm). It was also found that $MoSi_2$ grains in the SML-40 specimen (Fig. 2(c)) were significantly larger than that in the SMY-40 specimen. The results of the $MoSi_2$ grain size measurements on these two materials are plotted in the Fig. 2(d). It indicates that the mean grain size (d_m) of $MoSi_2$ in the SML-40 (1.95 μm) was nearly double of that in the SMY-40 composites (1.08 μm). This difference can be attributed to the different sintering conditions. The sintering temperature for the Lu_2O_3-doped materials was 100 °C higher than that used for the YAG-doped materials.

3.2. Electrical properties

Note that all the material properties mentioned in the following text are from the composites fabricated in an Ar atmosphere. The room-temperature electrical conductivity as a function of $MoSi_2$ volume fraction for YAG and Lu_2O_3-doped Si_3N_4–$MoSi_2$ is shown in Fig. 3. It shows that the electrical conductivity of the composites increased with $MoSi_2$ volume fraction in a manner typical for percolation systems as described below. At low $MoSi_2$ concentrations, the isolated $MoSi_2$ particles were dispersed in the insulating Si_3N_4 matrix and hence the electrical conductivity is very low. A steep rise of conductivity was seen when the $MoSi_2$ concentration reached a critical value, i.e. the percolation concentration, when the first three-dimensional conductive network occurred. At the percolation concentration, the distribution state of $MoSi_2$ particles changed from a dispersive distribution to a network distribution. Above the percolation threshold, the electrical conductivity, ranged from 10^2 to 10^5 Ω^{-1} cm^{-1}, increased slowly with the $MoSi_2$ content, which was related to the increase of the density of conductive percolating paths. Percolation of the $MoSi_2$ phase started at approximately 27 and 32 vol.% for the SMY and the SML composites, respectively. The difference in the percolation concentration was related to the difference in grain diameter of $MoSi_2$ phase in these two types of composites. As mentioned, the grain size of $MoSi_2$ in the Lu_2O_3-doped materials was twice as large as that in the YAG-doped composites. According to the geometrical percolation model presented by Malliaris and Turner,[30] the percolation concentration of a conductor–insulator type composite increases inversely with the ratio of diameters of insulating particles to conductive particles. In Yamada's experimental study,[13] it was shown that the percolation concentration of Si_3N_4–$MoSi_2$ composites is sensitive to the diameter ratio of the Si_3N_4 to $MoSi_2$ phase. A Si_3N_4–$MoSi_2$ composite con-

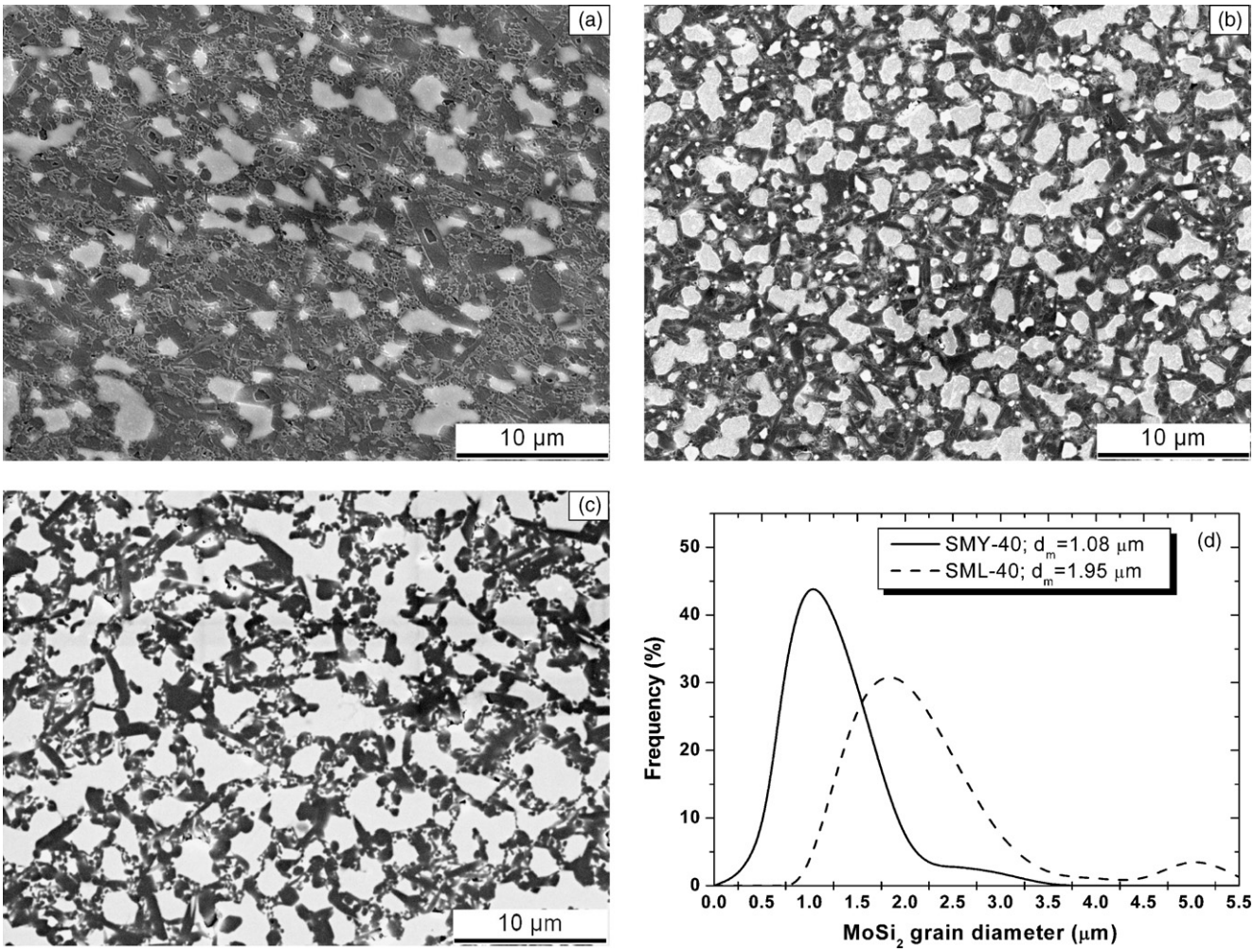

Fig. 2. SEM micrographs of the SMY-40 composites sintered in (a) N_2 and (b) Ar, and (c) the SML-40 composite sintered in Ar; (d) the histogram of the $MoSi_2$ grain diameter, measured by the linear intercept method, in SMY-40 and SML-40 composites sintered in Ar.

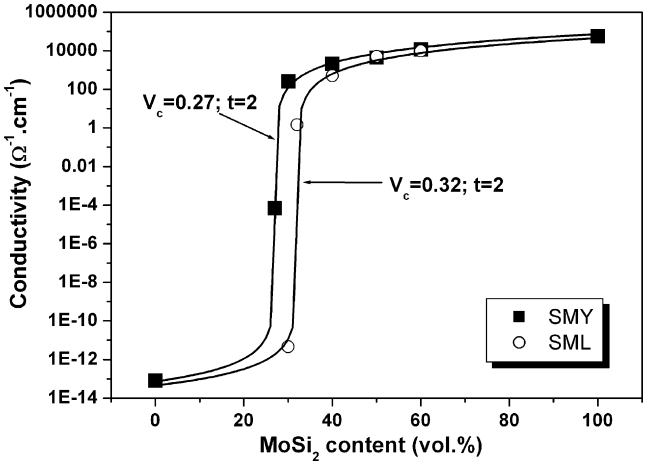

Fig. 3. Room-temperature electrical conductivity of the Si_3N_4–$MoSi_2$ composites containing $Y_2O_3 + Al_2O_3$ (SMY) or Lu_2O_3 (SML) as the sintering additives as a function of the $MoSi_2$ volume fraction; the data are fitted with GEM equation (solid line) with a t value of 2.

taining 30 wt.% $MoSi_2$ was changed from a good conductor ($\sim 10^{-2}\ \Omega$ cm) to an insulator ($\sim 10^{-10}\ \Omega$ cm) by decreasing the diameter ratio of Si_3N_4 to $MoSi_2$ particles from 10:1 to 3:1. Given the fact that the size of Si_3N_4 grains in both composites in the current study was very similar, the larger $MoSi_2$ grain size in the SML composites leads to a lower ratio of diameters of the insulating/conductive particles and therefore a higher percolation concentration in the SML composites. The obtained conductivity data was fitted with the general effective media (GEM) equation proposed by McLachlan et al.[31]:

$$\frac{f(\sigma_m^{1/t} - \sigma_{comp}^{1/t})}{\sigma_m^{1/t} + A\sigma_{comp}^{1/t}} + \frac{(1-f)(\sigma_p^{1/t} - \sigma_{comp}^{1/t})}{\sigma_p^{1/t} + A\sigma_{comp}^{1/t}} = 0 \quad (4)$$

where σ_{comp}, σ_m, σ_p are the electrical conductivities of the composite, the insulating phase (Si_3N_4) and the conductive phase ($MoSi_2$), respectively; f the volume fraction of the conductive phase; f_c the percolation concentration. A is equal to $f_c/(1-f_c)$. The critical exponent, t, is a phenomenological parameter that characterises the composite microstructure, which ranges normally between 1 and 4.49. The result of the fitting is shown as

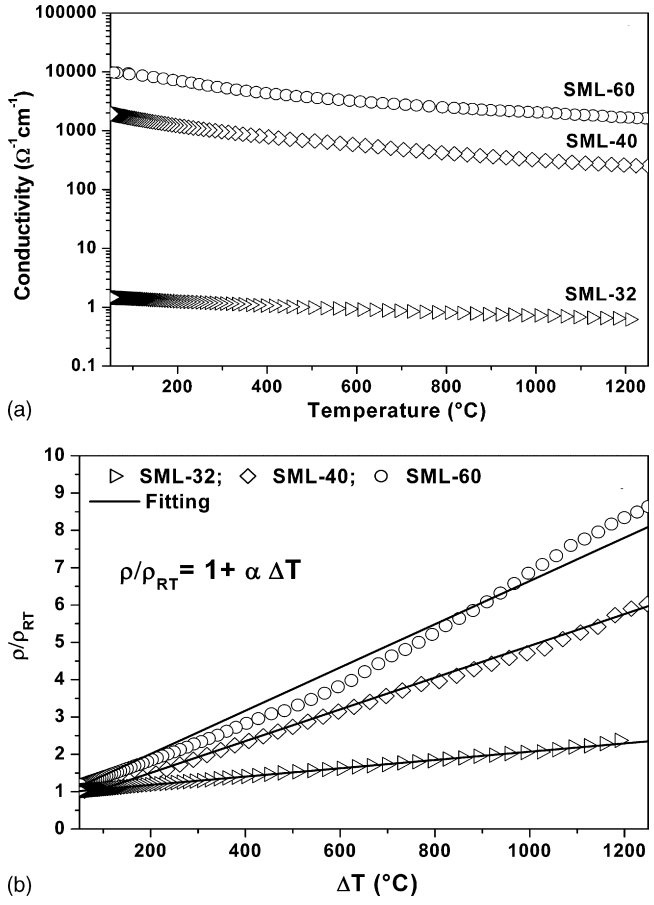

Fig. 4. (a) Electrical conductivity vs. temperature for the Si_3N_4–$MoSi_2$–Lu_2O_3 composites with 32 vol.% (SML-32), 40 vol.% (SML-40) and 60 vol.% (SML-60) $MoSi_2$; (b) plots of ρ/ρ_{RT} vs. ΔT, the slopes of the straight lines are equal to the temperature coefficient of resistivity (α).

solid lines in Fig. 3. A good correlation between the measured data and the theoretical prediction was obtained using a value of t of 2.0.

To use Si_3N_4–$MoSi_2$ composites in high-temperature electrical devices, it is important to consider its electrical properties at elevated temperatures. For the first time, we report the temperature dependence of the electrical conductivity of the Si_3N_4–$MoSi_2$–Lu_2O_3 composites at temperatures up to 1250 °C, as shown in Fig. 4(a). The composites containing 32, 40 and 60 vol.% $MoSi_2$ exhibited positive temperature coefficient of resistivity (PTCR) over the whole temperature range, which indicates that metallic-like electron conduction was the dominant conduction mechanism. Since the electrical conductivity of $MoSi_2$ ($\sim 10^5\ \Omega^{-1}\,cm^{-1}$) is 18 orders of magnitude higher than that of Si_3N_4 ($\sim 10^{-13}\ \Omega^{-1}\,cm^{-1}$), electrons are transported dominantly through the conductive $MoSi_2$ percolating paths. The temperature coefficient of resistivity (TCR) is one of the most important characteristic parameters for a conductor and it can be calculated according to the following equation[32]:

$$\frac{\rho}{\rho_{RT}} = 1 + \alpha \Delta T \tag{5}$$

where ρ is the electrical resistivity at a given temperature (T); ρ_{RT} the electrical resistivity at room temperature (T_{RT}); α the temperature coefficient of resistivity (TCR); ΔT is equal to $T - T_{RT}$. The TCRs of the composites were obtained from the slope of the ρ/ρ_{RT} versus ΔT plots, as shown in Fig. 4(b). The discrepancy of the data points from the straight lines in Fig. 4(b) may be due to the error induced by the surface oxidation during the measurements at high-temperatures. It was found that the TCRs of Si_3N_4–$MoSi_2$ composites increased with $MoSi_2$ volume fraction from $1.1 \times 10^{-3}\ °C^{-1}$ for the SML-32 composite to $4.3 \times 10^{-3}\ °C^{-1}$ and $5.8 \times 10^{-3}\ °C^{-1}$ for the SML-40 and the SML-60 composites, respectively. Similar behaviour was also observed in Al_2O_3–$MoSi_2$ composites.[33]

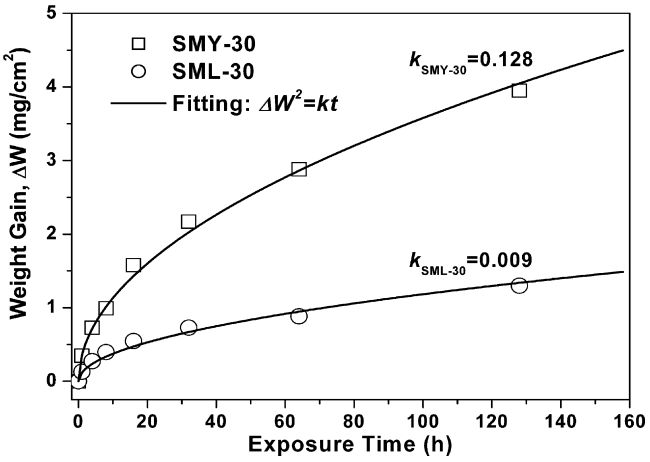

Fig. 5. Plots of the specific weight gain as a function of exposure time for the SMY-30 and the SML-30 composites oxidized at 1500 °C in air.

3.3. Oxidation behaviour

Fig. 5 shows the specific weight gain of the Si_3N_4 + 30 vol.% $MoSi_2$ composites doped with YAG (SMY-30) and Lu_2O_3 (SML-30) sintered in Ar during the exposure in air at 1500 °C as a function of oxidation time. The final specific weight gains after 128 h oxidation were 3.95 and 1.30 mg cm^{-2} for the SMY-30 and the SML-30 specimens, respectively. These results confirmed that the use of Lu_2O_3 as the sintering additive leads to an improvement in oxidation resistance for Si_3N_4–$MoSi_2$ composites. It has been reported that the Lu_2O_3-doped Si_3N_4 materials have an excellent oxidation resistance due to the high melting point and crystallisation of the grain boundary phase.[21,34] Our finding shows that the same is true for Si_3N_4–$MoSi_2$ composites. The oxidation behaviours of tested specimens approximately obeyed a parabolic law as described in the following equation:

$$\Delta W^2 = kt \tag{6}$$

where ΔW is the specific weight gain; t the exposure time and k is the parabolic oxidation rate constant at a given temperature. The parabolic rate constants, k, were obtained by fitting the weight gain data with Eq. (6), and were 0.128 and 0.009 $mg^2\,cm^{-4}\,h^{-1}$ for the SMY-30 and the SML-30 composites, respectively. The parabolic rate constant for the Lu_2O_3-doped Si_3N_4–$MoSi_2$ composite was about one order of magnitude smaller than that of the YAG-doped one. This is about one order magnitude higher than those of HIPed pure Si_3N_4[11] and HPed Lu_2O_3-

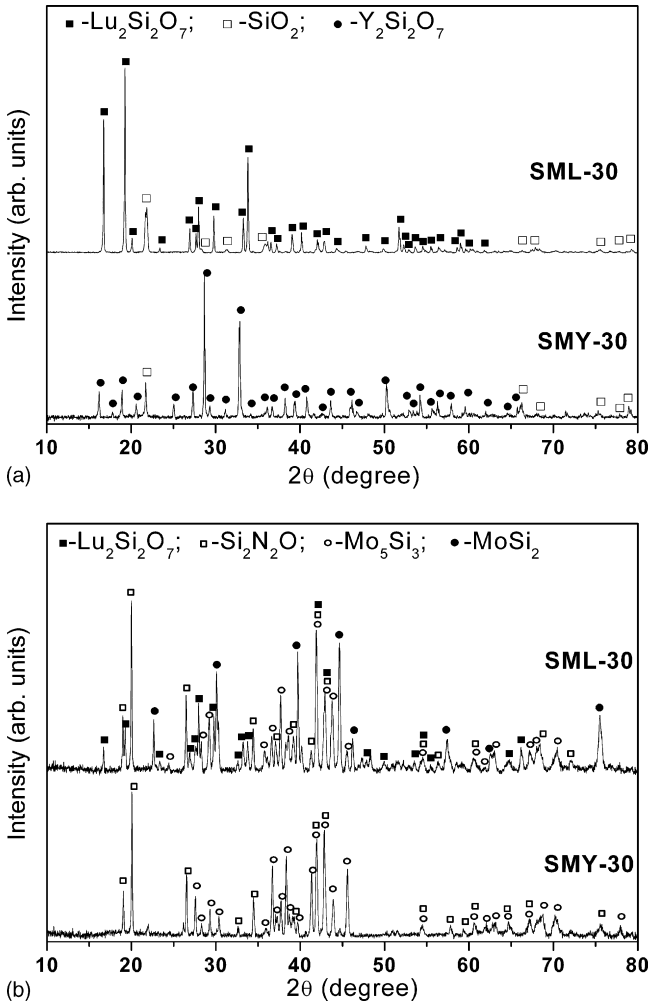

Fig. 6. X-ray diffraction patterns of (a) the oxidized surfaces and (b) after removing the oxidized layer for the SMY-30 and the SML-30 composites after oxidation at 1500 °C in air for 128 h.

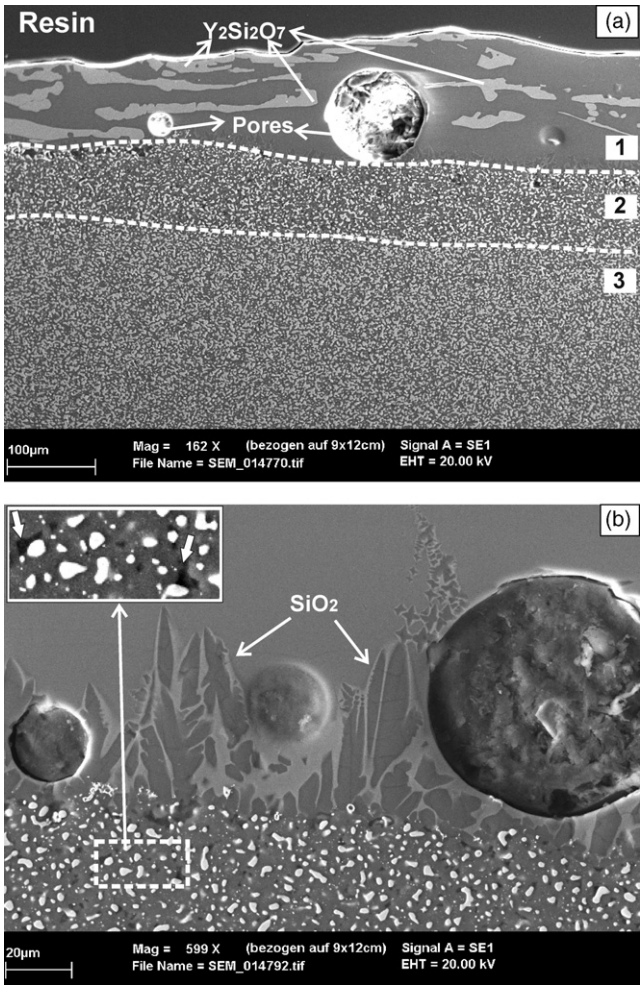

Fig. 7. (a) SEM micrographs of the polished cross-sections of the SMY-30 composites after oxidation at 1500 °C in air for 128 h. Three layers marked in (a) are: (1) the outer oxidized layer; (2) the $MoSi_2$-depleted zone; (3) the bulk. (b) The interface region between the outer oxidised layer and the bulk. The inset in (b) is the enlargement of the $MoSi_2$-depleted region with the arrows indicating the presence of voids.

doped Si_3N_4 materials.[21] However, it is difficult to compare the oxidation resistance of monolithic Si_3N_4 and Si_3N_4–$MoSi_2$ composites by only comparing the weight gain and the oxidation rate constant. This is because these two types of materials have different weight balances associated with different oxidation mechanisms.

The XRD analysis on the oxidized surfaces of the SMY-30 and the SML-30 specimens is presented in Fig. 6(a). The oxidized surfaces predominately consisted of crystallised $Y_2Si_2O_7$ or $Lu_2Si_2O_7$ for the SMY-30 and the SML-30 samples, respectively. In addition, crystallised SiO_2, cristobalite, was also observed in both cases and the intensity of the SiO_2 reflection peaks was stronger in the SML-30 than that in the SMY-30 sample. Mo_5Si_3 and Si_2N_2O phases were detected in the upper bulk after removing the oxidized surface layer, as shown in Fig. 6(b), which is consistent with Klemm's study.[12] It is proposed that Si_3N_4 and $MoSi_2$ in the surface region were directly oxidized to SiO_2 as described by the following equations:

$$Si_3N_4(s) + 3O_2(g) \rightarrow 3SiO_2(s) + 2N_2(g) \quad (7)$$

$$2MoSi_2(s) + 7O_2(g) \rightarrow 4SiO_2(s) + 2MoO_3(g) \quad (8)$$

The presence of $Y_2Si_2O_7$ or $Lu_2Si_2O_7$ crystals on the surfaces was the consequence of the migration of Y^{3+} or Lu^{3+} cations from the unoxidized bulk materials to the surface during the oxidation. The parabolic oxidation kinetics also indicates that the oxidation process was controlled by diffusion, including the inward diffusion of oxygen and outward diffusion of nitrogen and the additive species across the oxidation scale. These diffusion processes occurring during oxidation resulted in an oxidation scale with a complex multi-layered microstructure with a compositional gradient.[11,21]

The microstructure of the oxidation scale in the SMY-30 composite is shown in Fig. 7. Approximately three different layers from the outer surface to the bulk were distinguishable. (1) An outer oxidation layer in the YAG-doped composite mainly consisted of amorphous SiO_2 matrix and long-shaped $Y_2Si_2O_7$ crystals. The thickness of this scale was approximately 150 μm. Large pores, with diameter up to 100 μm, were found in this region as a result of N_2 released by the oxidation reactions. (2) A $MoSi_2$-depleted intermediate layer located between the

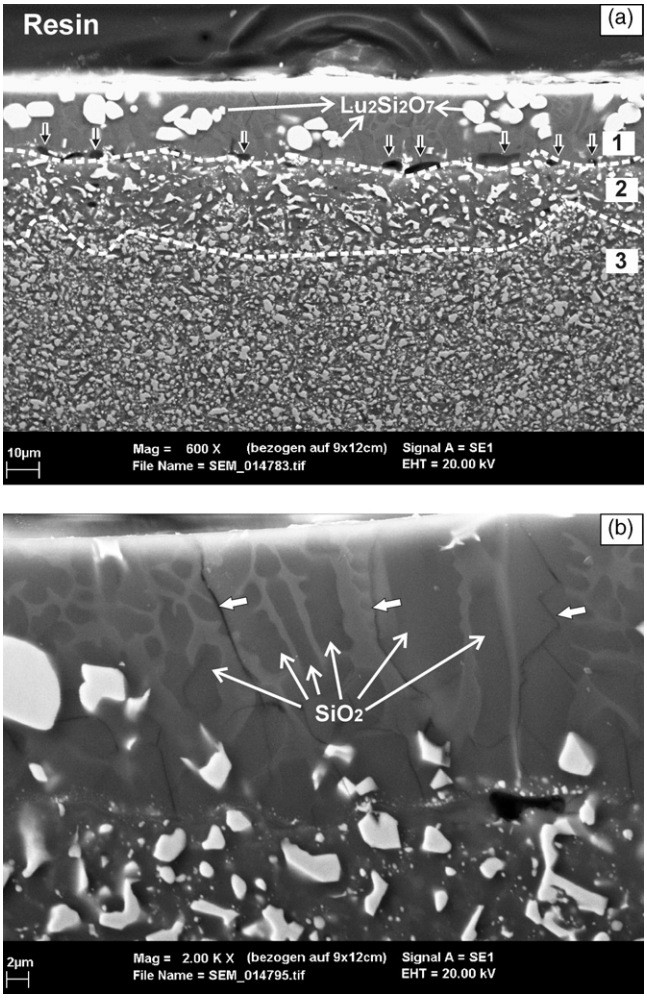

Fig. 8. (a) SEM micrographs of the polished cross-sections of the SML-30 composites after oxidation at 1500 °C in air for 128 h. Three layers marked in (a) are: (1) the outer oxidized layer; (2) the $MoSi_2$-depleted zone; (3) the bulk. (b) The high magnification image of the outer oxidized layer. The arrows in (a) indicate the pores trapped in the bottom of the oxidized layer and the arrows in (b) highlight the cracks present in the oxidized layer.

outer oxidation scale and the bulk was observed. Part of the $MoSi_2$ content was oxidized, resulting in a lower $MoSi_2$ content in this region compared with that in the unoxidized samples. The small voids left by outward diffusion of the Y^{3+} and Al^{3+} cations[17] were observed in this region in the SMY-30 specimen, as shown in Fig. 7(b). Additionally, a layer containing dendrite-shaped SiO_2 crystals growing in the direction perpendicular to the surface was located between the outer oxidation scale and the $MoSi_2$-depleted zone (Fig. 7(b)). The presence of the crystallized SiO_2 intermediate layer may reduce the kinetic of the oxygen diffusion towards the bulk and improve the oxidation resistance of Si_3N_4–$MoSi_2$ composites. (3) The bulk microstructure similar to that prior to oxidation.

A similar multi-layered microstructure can be seen in the SML-30 composite as well, as shown in Fig. 8. Compared to the SMY-30 specimen, (1) the outer oxidation layer in the Lu_2O_3-doped specimen (SML-30) was much thinner, i.e. ~20 μm. This also indicates that the oxidation rate of the composites containing Lu_2O_3 was lower than that of the YAG-doped composites. Equiaxed $Lu_2Si_2O_7$ crystals were found embedded in this layer and small pores were seen trapped at the interface between the oxidized layer and the $MoSi_2$-depleted zone in the SML-30 sample. Since the outer oxidation layer in the SML-30 specimen was relatively thin, the SiO_2 crystals grew through the whole oxidation scale, as shown in Fig. 8(b). The large volume change associated with the crystallisation of SiO_2 leads to cracking in the oxidation layer in the SML-30 composite. (2) The $MoSi_2$-depleted intermediate layer in the SML-30 sample, with a thickness of ~20 μm, was also much thinner than that in the SMY-30 specimen (~100 μm). Moreover, the small voids present in the $MoSi_2$-depleted zone in the SMY-30 specimen were not observed in the SML-30 specimen, which is probably related to the crystallisation of the grain boundaries in the SML-30 composite, which significantly limited the diffusion rate of Lu^{3+} cations. (3) Finally the bulk microstructure as the unoxidized state.

Based on the microstructural analysis, it might be concluded that the most critical step influencing the oxidation process of the Si_3N_4–$MoSi_2$ composites was the diffusion of oxygen across the protective surface layer at elevated temperatures.[35] Therefore a low oxygen diffusion coefficient of the oxidation scale is beneficial for the improvement of the oxidation resistance. It has been reported that pure silica has the lowest oxygen diffusion coefficient.[34] Addition of additive cations, such as Al^{3+}, Y^{3+} or Lu^{3+}, into the silica layer would lower the eutectic temperatures and lead to an increase of oxygen diffusion into the materials. The lowest eutectic temperature in Si_3N_4–SiO_2–Y_2O_3 system is 1450 °C and addition of Al_2O_3 will lower this further,[36] which is significantly lower than that reported of materials only containing Lu_2O_3 as the sintering additive (>1750 °C).[34] Therefore, the oxygen diffusion coefficient should be much smaller in the Lu_2O_3-doped composite. Furthermore, the extensive crystallisation in the oxidation scale of the SML-30 sample significantly reduced the oxygen diffusion coefficient and hence the Lu_2O_3-doped composite (SML-30) was much more resistant to oxidation than the one containing YAG (SMY-30). Most of the oxygen that diffused through the outer oxidation scale was consumed by the oxidation reaction at the interface between the oxidation layer and the bulk. However, some residual oxygen penetrated via the grain boundaries into the bulk material, leading to the formation of the $MoSi_2$-depleted zone beneath the outer oxidation layer. The crystallised grain boundary phase in the Lu_2O_3-doped material (SML-30) helped to reduce the oxygen penetration and thus the thickness of the $MoSi_2$-depleted zone in the SML-30 specimen was much smaller compared to that in the SMY-30 specimen. The low mobility of additive ions in the crystallised grain boundary region of SML-30 also restricted the outwards diffusion of Lu^{3+} cations, which was driven by the chemical gradient between the oxidation scale and the bulk. This resulted in a less severe microstructure modification in the $MoSi_2$-depleted zone, e.g. no voids or inhomogeneous grain boundary region, in the Lu_2O_3-doped composites. The coefficient of thermal expansion (CTE) is an important issue for designing an environmental barrier coating (EBC). Spalling of the oxidation layers was not observed in both composites and therefore we can assume that the CTEs of oxidation layers match that of the bulk.

4. Conclusions

Si_3N_4–$MoSi_2$ composites with YAG and Lu_2O_3 as sintering additives were produced by hot pressing in N_2 and Ar atmospheres. The electrical and oxidation properties were studied and the following results were obtained:

(i) $MoSi_2$ phase reacted with N_2 gas to form Mo_5Si_3 during hot pressing. Such reaction could be suppressed by using Ar as the sintering atmosphere.
(ii) The grain boundary phase of the YAG-doped Si_3N_4–$MoSi_2$ was mostly amorphous. However, the use of Lu_2O_3 as the sintering additive produced crystallised $Lu_2Si_2O_7$ and Si_2N_2O at the grain boundary phases.
(iii) The room temperature electrical conductivity data of the YAG and Lu_2O_3-doped Si_3N_4–$MoSi_2$ composites were successful fitted using GEM equation. The percolation concentrations were ~27 and ~32 vol.% of $MoSi_2$ for the SMY and SML composites, respectively. The composites with $MoSi_2$ content above the percolation concentration exhibited positive temperature coefficient of resistivity (PTCR) and metallic-like conduction was the dominant conduction mechanism.
(iv) Parabolic oxidation kinetic was found in both YAG and Lu_2O_3-doped Si_3N_4–$MoSi_2$ composites. The parabolic oxidation rate constants were dependent on the type of sintering additive. The Lu_2O_3-doped Si_3N_4–$MoSi_2$ composite had an oxidation rate constant one order of magnitude smaller than that of the YAG-doped one.
(v) A higher eutectic temperature and extensive crystallisation of the outer oxidation layer in SML composites was responsible for the superior oxidation resistance.

Acknowledgements

This work was funded by Swiss Commission for Technology and Innovation under TopNano 21 program (grant No. 6620.1). The authors are grateful to H.J. Schindler for his technical assistance.

References

1. Zerr, A., Miehe, G., Serghiou, G., Schwarz, M., Kroke, E., Riedel, R. *et al.*, Synthesis of cubic silicon nitride. *Nature*, 1999, **400**, 340–342.
2. Blugan, G., Hadad, M., Janszak-Rusch, J., Kuebler, J. and Graule, T., Microstructure, mechanical properties and fractography of commercial silicon nitride–titanium nitride composites for wear applications. *J. Am. Ceram. Soc.*, 2005, **88**, 926–933.
3. Gogotsi, Y. G., Review: particulate silicon nitride based composite. *J. Mater. Sci.*, 1994, **29**, 2541–2556.
4. Kawano, S., Takahashi, J. and Shimada, S., Fabrication of TiN/Si_3N_4 ceramics by spark plasma sintering of Si_3N_4 particles coated with nanosized TiN prepared by controlled hydrolysis of Ti(O-*i*-C_3H_7)$_4$. *J. Am. Ceram. Soc.*, 2003, **86**, 701–705.
5. Huang, J. L., Chen, S. Y. and Lee, M. T., Microstructure, chemical aspects and mechanical properties of TiB_2/Si_3N_4 and TiN/Si_3N_4 composites. *J. Mater. Res.*, 1994, **9**, 2349–2354.
6. Petrovskya, V. Y. and Rakb, Z. S., Densification, microstructure and properties of electroconductive Si_3N_4-TaN composites. Part I. Densification and microstructure. *J. Eur. Ceram. Soc.*, 2001, **21**, 219–235.
7. Petrovskya, V. Y. and Rakb, Z. S., Densification, microstructure and properties of electroconductive Si_3N_4-TaN composites. Part II. Electrical and mechanical properties. *J. Eur. Ceram. Soc.*, 2001, **21**, 237–244.
8. Peni, E., Crampon, J. and Duclos, R., Creep and microstructure of TiC particulate Si_3N_4-based composites. *J. Eur. Ceram. Soc.*, 1991, **8**, 311–318.
9. Petrovic, J. J., Pena, M. I., Reimans, I. E., Sandlin, M. S., Conzone, S. D., Kung, H. H. *et al.*, Mechanical behaviour of $MoSi_2$ reinforced-Si_3N_4 Matrix composites. *J. Am. Ceram. Soc.*, 1997, **80**, 3070–3076.
10. Petrovic, J. J., Pena, M. I. and Kung, H. H., Fabrication and microstructure of $MoSi_2$ reinforced-Si_3N_4 matrix composites. *J. Am. Ceram. Soc.*, 1997, **80**, 1111–1116.
11. Klemm, H., Taut, C. and Wötting, G., Long-term stability of nonoxide ceramics in an oxidation environment at 1500 °C. *J. Eur. Ceram. Soc.*, 2003, **23**, 619–627.
12. Klemm, H., Herrmann, M. and Schubert, C., Silicon nitride composites materials with an improved high temperature oxidation resistance. *Ceram. Eng. Sci. Proc.*, 1997, **18**, 615–623.
13. Yamada, K. and Kamiya, N., High temperature mechanical properties of Si_3N_4–$MoSi_2$ and Si_3N_4–SiC composites with network structures of second phases. *Mater. Sci. Eng.*, 1999, **A261**, 270–277.
14. Sciti, D., Guicciardi, S. and Bellosi, A., Microstructure and properties of Si_3N_4–$MoSi_2$ composites. *J. Ceram. Proc. Res.*, 2002, **3**, 87–95.
15. Gauckler, L. J., Hohnke, H. and Tien, T. Y., The system of Si_3N_4–SiO_2–Y_2O_3. *J. Am. Ceram. Soc.*, 1980, **63**, 35–37.
16. Cinihulk, M. K. and Gareth, T., Fabrication and secondary-phase crystallization of rare-earth disilicate-silicon nitride ceramics. *J. Am. Ceram. Soc.*, 1992, **75**, 2037–2043.
17. Gogotsi, Y. G. and Backhaus-Ricoult, M., Identification of oxidation mechanism in silicon nitride ceramics by transmission electron microscopy studies of oxide scales. *J. Mater. Res.*, 1995, **10**, 2306–2321.
18. Strecker, K., Gonzaga, R., Ribeiro, S. and Hoffmann, M. J., Substitution of Y_2O_3 by a rare earth oxide mixture as sintering additive of Si_3N_4 ceramics. *Mater. Lett.*, 2000, **45**, 39–42.
19. Cinihulk, M. K. and Thomas, G., Oxidation of rare-earth disilicate-silicon nitride ceramics. *J. Am. Ceram. Soc.*, 1992, **75**, 2044–2049.
20. Cinihulk, M. K. and Gareth, T., Strength and creep behaviour of rare-earth disilicate-silicon nitride ceramics. *J. Am. Ceram. Soc.*, 1992, **75**, 2050–2055.
21. Guo, S., Hirosaki, N., Nishimura, T., Yamamoto, Y. and Mitomo, M., Hot pressed silicon nitride with Lu_2O_3 additives: oxidation and its effect on strength. *J. Am. Ceram. Soc.*, 2003, **86**, 1900–1905.
22. Guo, S., Hirosaki, N., Yamamoto, Y., Nishimura, T. and Mitomo, M., Improvement of high-temperature strength of hot-pressed sintering silicon nitride with Lu_2O_3 addition. *Scr. Mater.*, 2001, **45**, 867–874.
23. Guo, S., Hirosaki, N., Yamamoto, Y., Nishimura, T., Kitami, Y. and Mitomo, M., Microstructural characterization and high-temperature strength of hot-pressed silicon nitride ceramics with Lu_2O_3 additives. *Phil. Mag. Lett.*, 2003, **83**, 357–365.
24. EN 623-3. Advanced technical ceramics – monolithic ceramics – general and textural properties. Part 5. Determination of grain size and grain distribution (characterized by the Linear Intercept Method); 2001.
25. Van der Pauw, L. J., A method of measuring specific resistivity and Hall effect of arbitrary shape. *Philips Res. Repts.*, 1958, **13**, 1–9.
26. ASTM F 43-93. Standard test methods for resistivity of semiconductor materials, *Annual Book of ASTM Standards*, 1993, **10.5**, 33–38.
27. Kao, M. Y., Properties of silicon-nitride molybdenum disilicide composites. *J. Am. Ceram. Soc.*, 1993, **76**, 2879–2883.
28. Barin, I. and Platzki, G., *Thermochemical data of pure substances* (*3rd ed.*). VCH Verlagsgesellschaft, Weinheim, 1995, pp. 1079–1503.
29. Heikinheimo, E., Kodentsov, A., Van Beek, J. A., Klomp, J. T. and Van Loo, F. J. J., Reactions in the systems Mo–Si_3N_4 and Ni–Si_3N_4. *Acta Metall. Mater.*, 1992, **40**, S111–S119.
30. Malliaris, A. and Turner, D. T., Influence of particle size on the electrical resistivity of compacted mixtures of polymeric and metallic powders. *J. Appl. Phys.*, 1971, **42**, 614–618.
31. McLachlan, D. S., Blaszkiewicz, M. and Newnham, R. E., Electrical resistivity of composites. *J. Am. Ceram. Soc.*, 1990, **73**, 2187–2203.
32. Askeland, D. R. and Phulè, P. P., *The science and engineering of materials* (*4th ed.*). Thomson Brooks/Col, Pacific Grove, CA, 2003, p. 800.

33. Köbel, S., Pluschke, J., Vogt, U. and Graule, T. J., $MoSi_2$–Al_2O_3 electroconductive ceramic composites. *Ceram. Int.*, 2004, **30**, 2105–2110.
34. Hirosaki, N., Yamamoto, Y., Nishimura, T. and Mitomo, M., Phase relationships in Si_3N_4–SiO_2–Lu_2O_3 system. *J. Am. Ceram. Soc.*, 2002, **86**, 2861–2863.
35. Jacobson, N., Corrosion of silicon-based ceramics in combustion environments. *J. Am. Ceram. Soc.*, 1993, **76**, 3–28.
36. Hampshire, S., The role of additives in the pressureless sintering of nitrogen ceramics for engine applications. *Metals Forum*, 1984, **7**, 162–170.